

See discussions, stats, and author profiles for this publication at: <https://www.researchgate.net/publication/6377531>

# NLOPredict: Visualization and data analysis software for nonlinear optics

ARTICLE *in* JOURNAL OF COMPUTATIONAL CHEMISTRY · SEPTEMBER 2007

Impact Factor: 3.59 · DOI: 10.1002/jcc.20706 · Source: PubMed

---

CITATIONS

19

---

READS

36

9 AUTHORS, INCLUDING:



[John Perry](#)

University of North Carolina at Chapel Hill

11 PUBLICATIONS 245 CITATIONS

SEE PROFILE



[Randy Heiland](#)

Indiana University Bloomington

32 PUBLICATIONS 370 CITATIONS

SEE PROFILE

# *NLOPredict*: Visualization and Data Analysis Software for Nonlinear Optics

ANDREW J. MOAD,<sup>1</sup> CHARLES W. MOAD,<sup>2</sup> JOHN M. PERRY,<sup>1</sup> RONALD D. WAMPLER,<sup>1</sup> G. SCOTT GOEKEN,<sup>1</sup>  
 NATHAN J. BEGUE,<sup>1</sup> TIAN SHEN,<sup>1</sup> RANDY HEILAND,<sup>2</sup> GARTH J. SIMPSON<sup>1</sup>

<sup>1</sup>Department of Chemistry, Purdue University, West Lafayette, Indiana 47907

<sup>2</sup>Scientific Data Analysis Lab, Pervasive Technology Labs, Indiana University, Indianapolis, Indiana 46202

Received 3 November 2006; Revised 11 January 2007; Accepted 21 January 2007

DOI 10.1002/jcc.20706

Published online 20 April 2007 in Wiley InterScience (www.interscience.wiley.com).

**Abstract:** A data analysis and visualization program was developed to assist in the interpretation of second-order nonlinear optical (NLO) processes, including vibrational sum-frequency generation and electronically resonant second harmonic generation. A novel diagrammatic approach allows concise visual representations of the resonant NLO molecular response. By mapping the predicted NLO response as a function of molecular orientation, molecular modeling results can be combined with experimental measurements for orientational analysis. A method is developed and implemented to predict the nonlinear optical properties of the amide backbones in complete proteins with known structures. *NLOPredict* is available for most computer operating systems from <http://sda.iu.edu/nlopredict/>.

© 2007 Wiley Periodicals, Inc. J Comput Chem 28: 1996–2002, 2007

**Key words:** second harmonic generation; sum-frequency generation; nonlinear optics; hyperpolarizability; molecular orientation

## Introduction

As the diversity of nonlinear optical measurements grows and expands so does the need for methods to facilitate interpretation of complex samples.<sup>1–5</sup> In this work, we describe the development of a software package (*NLOPredict*) designed to help address this growing need.

A nonlinear optical process involves multiple photons interacting simultaneously within a molecule or material. Nonlinear optical measurements can yield rich structural information complementing more traditional optical approaches. The process of sum frequency generation (SFG) is depicted in Figure 1 under conditions of resonance-enhancement at the sum frequency ( $\omega_3$ ) and resonant with one of the incident optical frequencies (in this case,  $\omega_2$ ). Second harmonic generation (SHG) arises when the two incident frequencies are equal and is a specific case of SFG.

Quantum mechanically, second order NLO processes are described by rank 3 tensors. At the molecular level, general frequency-domain sum-over-states equations for nonlinear optical processes have recently been shown to reduce down to direct products of lower order effects without introducing additional assumptions or approximations.<sup>6</sup> For example, a rank 3 tensor describing a three photon process can be written as a sum of products of rank 2 tensors and vectors.<sup>6,7</sup> This simplification approach

is exemplified in eq. (1), which describes SFG resonant with  $\omega_3$ .

$$\beta^{(2)}(-\omega_3; \omega_1, \omega_2) = -S_\omega \mu_{0q}^{(0)} \otimes \alpha_{q0}^{(1)} \quad (1)$$

The nonlinear polarizability tensor  $\beta^{(2)}$  can be interpreted at the molecular level as a coherent combination of the tensor for two-photon absorption (TPA)  $\alpha^{(1)}$  and the transition moment for one-photon emission  $\mu^{(0)}$  when resonant with the sum frequency. Under conditions of resonance-enhancement with one of the incident frequencies (e.g.,  $\omega_2$ ), the nonlinear polarizability reduces to the direct product of the anti-Stokes Raman tensor and the transition moment,  $\beta^{(2)} = -S_\omega \alpha_{0q}^{(1)} \otimes \mu_{q0}^{(0)}$ . The lineshape function  $S_\omega$  has units of energy<sup>-1</sup> and will be complex-valued on resonance.

Nonlinear optical measurements are almost invariably performed on assemblies of many molecules rather than on individual

**Correspondence to:** R. Heiland; e-mail: [heiland@indiana.edu](mailto:heiland@indiana.edu) or G. J. Simpson; e-mail: [gsimpson@purdue.com](mailto:gsimpson@purdue.com)

Contract/grant sponsor: NSF; contract/grant number: CHE0316177

Contract/grant sponsors: Research Corporation (Research Innovation Award, Cottrell Scholar Award), Camille and Henry Dreifus Foundation (New Faculty Award), Eli Lilly (New Untenured Faculty Award), Endowment (IPCRS Initiative grant)

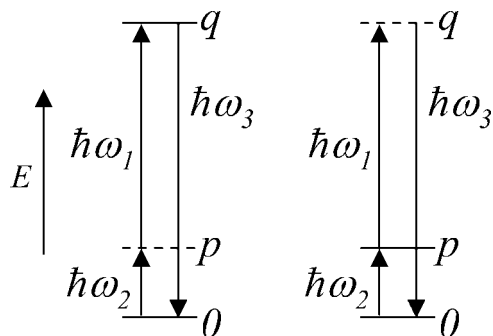


**Figure 1.** Energy level diagrams for common second-order nonlinear optical processes. Left: Sum-frequency generation resonant at the sum-frequency. Right: Sum-frequency generation with resonant-enhancement with one of the incident beams.

molecules, such that the macroscopic NLO susceptibility of a surface layer or material arises from the coherent summation of all of the molecular tensors. In an oriented assembly, the individual molecules will adopt a distribution in orientations. To describe the macroscopic response in an ultrathin surface film, the tensor for each molecule in its local coordinate system is projected onto a surface coordinate system through orientational averages (e.g., using Euler angles as defined in Fig. 2).

$$\chi_{ijk}^{(2)} = \sum_{i'j'k'=x'y'z'} N_s \langle R_{Ii'} R_{Jj'} R_{Kk'} \rangle \beta_{i'j'k'}^{(2)} \quad (2)$$

In eq. (2),  $N_s$  is the number density of chromophores and  $R_{\Lambda\lambda'}$  are elements of the Euler rotation matrix relating the molecular coordinate system to the macroscopic coordinate system.<sup>7</sup>

In practice, the majority of surface measurements using second-order methods are performed for macroscopic surfaces exhibiting  $C_\infty$  symmetry. Averaging over a uniform distribution in the Euler angle  $\phi$  reduced the number of unique nonzero elements to only seven for SFG and four for SHG. For an achiral film with  $C_{\infty v}$  symmetry, only four unique  $\chi^{(2)}$  tensor elements remain for SFG and three for SHG. However, each of these nonzero elements generally contains contributions from all nonzero elements of the molecular tensor (as many as 27 unique elements) and several independent orientational averages. If the molecular symmetry is sufficiently high, the orientational averages are easily tractable.<sup>8</sup> However, in molecular systems of low symmetry, analytical relationships connecting the molecular frame to the macroscopic frame can become cumbersome<sup>7,9,10</sup> and computational approaches become attractive alternatives.

## Computational Methods

NLOPredict is programmed in Python, which is freely available for common computer operating systems. NLOPredict is developed as a plug-in to the open-source protein visualization tool, Chimera, which is developed by the Computer Graphics Lab of the University of California, San Francisco.<sup>11</sup> Chimera is primarily written in Python, which is bundled together with its installation program.

Chimera is utilized by NLOPredict as a molecular viewer and to provide orientation control over a molecule.

Molecular modeling calculations were performed for disperse red 19 (DR-19) and *N*-methyl acetamide (NMA) using Gaussian 98.<sup>12</sup> For electronic transitions, geometry optimization was performed using the unrestricted semi-empirical AM1 basis set. A restricted ZINDO calculation for 100 electronic excited states was used to calculate the transition dipole moment and transition two-photon polarizability tensor for the state of experimental interest. Vibrational modes required a higher level of theory for reliable tensor data. Geometry optimizations were performed using the rb3lyp/6-311++g(d,p) basis set with the keyword verytight and ultrafine integration. Vibrational transition moments and Raman polarizability tensors were calculated under the same basis set and integration conditions with keywords Raman, iop(7/33=1) and polar.

## Tensor Visualization

An important first step in interpreting NLO measurements of molecules and macromolecular assemblies is development of intuitive descriptions of optical nonlinearity at the molecular level. A recently-developed diagrammatic representation of the resonant  $\beta^{(2)}$  tensor has been incorporated into NLOPredict.<sup>13</sup> As described in introduction section, a resonant  $\beta^{(2)}$  tensor can be expressed as a direct product of a transition moment and a rank 2  $\alpha^{(1)}$  tensor describing either Raman (e.g., for vibrational-SFG) or two-photon absorption (e.g., for electronically resonant SHG). The polarizability tensors  $\alpha^{(1)}$  for TPA and Raman can be separated into symmetric and antisymmetric parts. The symmetric tensor can be diagonalized to generate the eigenvalues and eigenvectors, which contain the same information as the original symmetric  $3 \times 3$  matrix. Representations of these tensors overlaid on the corresponding molecules are shown in Figure 3 for the  $S_0 \rightarrow S_1$  electronic transition at  $\sim 500$  nm in DR-19 and the  $NV_1 \pi \rightarrow \pi^*$  transition in (NMA). Transition dipole moments  $\mu^{(0)}$  are illustrated by vectors (yellow arrows). The symmetric transition polarizability tensors  $\alpha^{(1)}$  can be visualized by the

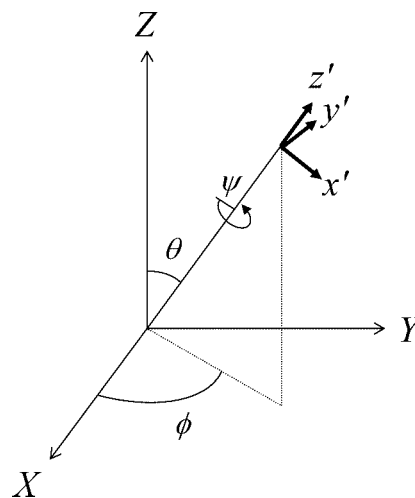


**Figure 2.** Euler angles ( $\theta, \psi, \phi$ ) relating the molecular ( $x', y', z'$ ) and macroscopic ( $X, Y, Z$ ) coordinate systems.

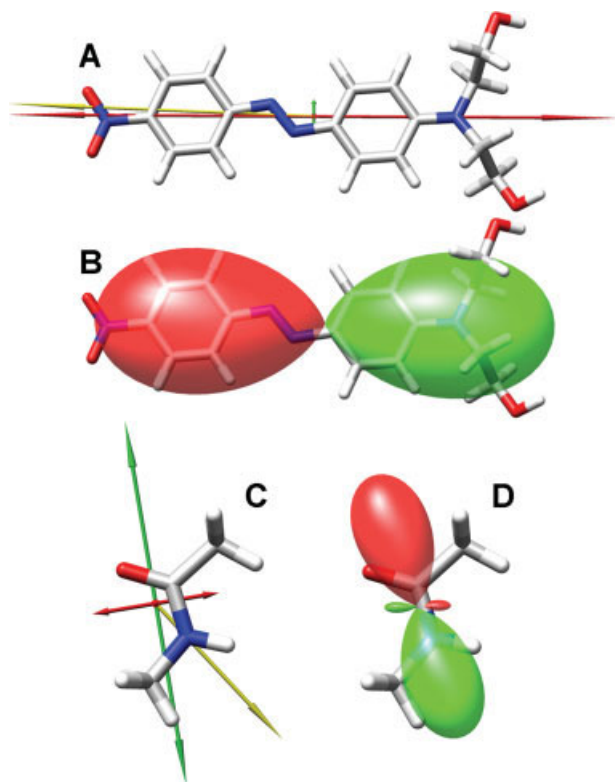


**Figure 3.** Two equivalent visual representations of the molecular tensors for SHG in DR-19 (A and B) and NMA (C and D). The arrow representation (A and C) displays the transition moment (yellow) and the polarizability tensor (red = negative; green = positive), which can be projected on any coordinate systems. The hyperellipsoid representation (B and D) displays the full rank 2 tensor (red = negative; green = positive). [Color figure can be viewed in the online issue, which is available at [www.interscience.wiley.com](http://www.interscience.wiley.com).]

glyphs indicating the eigenvectors. The magnitudes and signs of the principal elements (i.e., eigenvalues) are indicated by the lengths and colors of the double-sided arrows (red = negative; green = positive). Projection of these arrows on any arbitrary Cartesian coordinate system allows construction of the signs and magnitudes of all nonzero elements within the molecular tensor in that coordinate system.<sup>13</sup>

A second visualization option is also available in *NLOPredict*, in which hyperellipsoids are generated by mapping the magnitudes and signs of the nonlinear polarizability tensors as functions of direction. The magnitude of the surface contour along any axis corresponds to the efficiency of generating a nonlinear optical field polarized along that same axis when driven by coparallel incident fields. This option is available for tensors expressed as direct products of lower order effects [e.g., as in eq. (1)] and for full nonlinear polarizability tensors (e.g., from quantum chemical calculations in the zero-frequency limit). The hyperellipsoid representations are also shown in Figure 3 for electronic transitions in DR-19 and NMA.

### Plotting and Euler Angles

The macroscopic NLO response usually depends on the collective interactions of many chromophores through orientational

averages. Several different algorithms have been incorporated into *NLOPredict* to assist in qualitatively and quantitatively bridging macroscopic measurements and microscopic structure.

*NLOPredict* allows visualization of the complete set of microscopic and macroscopic tensor elements as a function of molecular orientation, shown in Figure 4 for DR-19. The *NLOPredict* window displays the three Euler angles connecting the macroscopic coordinate system for an assembly with  $C_\infty$  symmetry to the molecular coordinate system. Initially, a molecular file is opened in a particular coordinate system with all three Euler angles equal to zero. As the molecule is rotated in the viewing window, the Euler angles will change as the molecular orientation changes, with the Z-axis oriented out of the screen. At a given orientation, the nonlinear optical tensor within the molecular frame  $\beta^{(2)}$  and the macroscopic  $\chi^{(2)}$  tensor from a uniaxially oriented assembly about the Z-axis are plotted in the *NLOPredict* window as bar charts. The length of a bar in a graph indicates the value of a particular tensor element.

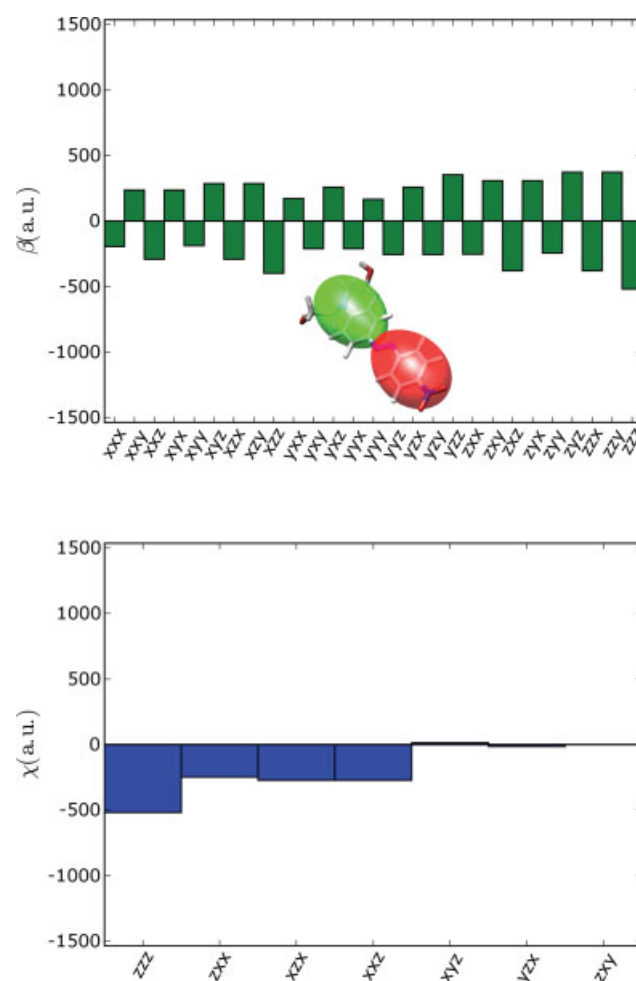


**Figure 4.** Molecular  $\beta^{(2)}$  (top) and macroscopic  $\chi^{(2)}$  tensor (bottom) elements for SHG resonant at the second harmonic frequency with the  $S_0 \rightarrow S_1$  electronic transition in DR-19. The long axis of the molecule is tilted  $45^\circ$  out of the plane of the page. [Color figure can be viewed in the online issue, which is available at [www.interscience.wiley.com](http://www.interscience.wiley.com).]

The molecular and macroscopic tensors update in real time as the molecule is rotated within the viewing window. Although the Euler angles depend on the initial coordinate system in which the molecular tensor is defined, the set of  $\beta^{(2)}$  and  $\chi^{(2)}$  tensor elements are independent of the particular selection of molecular coordinates.

An alternative complementary approach is to plot the nonlinear optical response of a single macroscopic tensor element or a combination of tensor elements at all possible orientations. Experimentally measured values for the  $\chi^{(2)}$  tensor elements or combinations thereof correspond to slices through the contour plots. Examples and applications of these representations are described in more detail in the following section.

It is common to encounter experimental situations in which the molecular orientation distribution is either very narrow (e.g., crystals, self-assembled monolayers, etc.) or very broad (e.g., EFISH measurements, physisorbed films, etc.), both of which can be modeled by *NLOPredict*. The first model is a  $\delta$ -function distribution for  $\theta$  and  $\psi$ , which is experimentally consistent with a highly oriented sample exhibiting a narrow distribution in orientation angles. The second model is one developed for describing the macroscopic NLO response in the weak orientation limit.<sup>14</sup> This limit is ubiquitous in

both EFISH measurements and in many surface measurements. In the limit of weak orientational order, it is assumed that there is an axis within the molecule (i.e., a director) about which the distribution in  $\psi$  is random and the distribution in  $\theta$  is broad (specifically, only the first Legendre moment is significant). The contour plot in the weak orientation limit corresponds to the macroscopic response as a function of the particular selection of the director (positioned along the Z-axis of the molecular viewing window). In an EFISH experiment, the director will always coincide with the axis containing the permanent dipole.

### Using *NLOPredict* for Data Analysis

An important application of *NLOPredict* is in the interpretation of experimental polarization measurements. Combining experimental measurements with molecular-level tensor inputs (e.g., from modeling calculations) allows calculation of maps of molecular orientation distributions in  $\theta$  and  $\psi$  consistent with a given data set.

An example of this procedure is shown in Figure 5 for SHG measurements of DR-19 at the glass/propanol solution interface.<sup>15</sup>

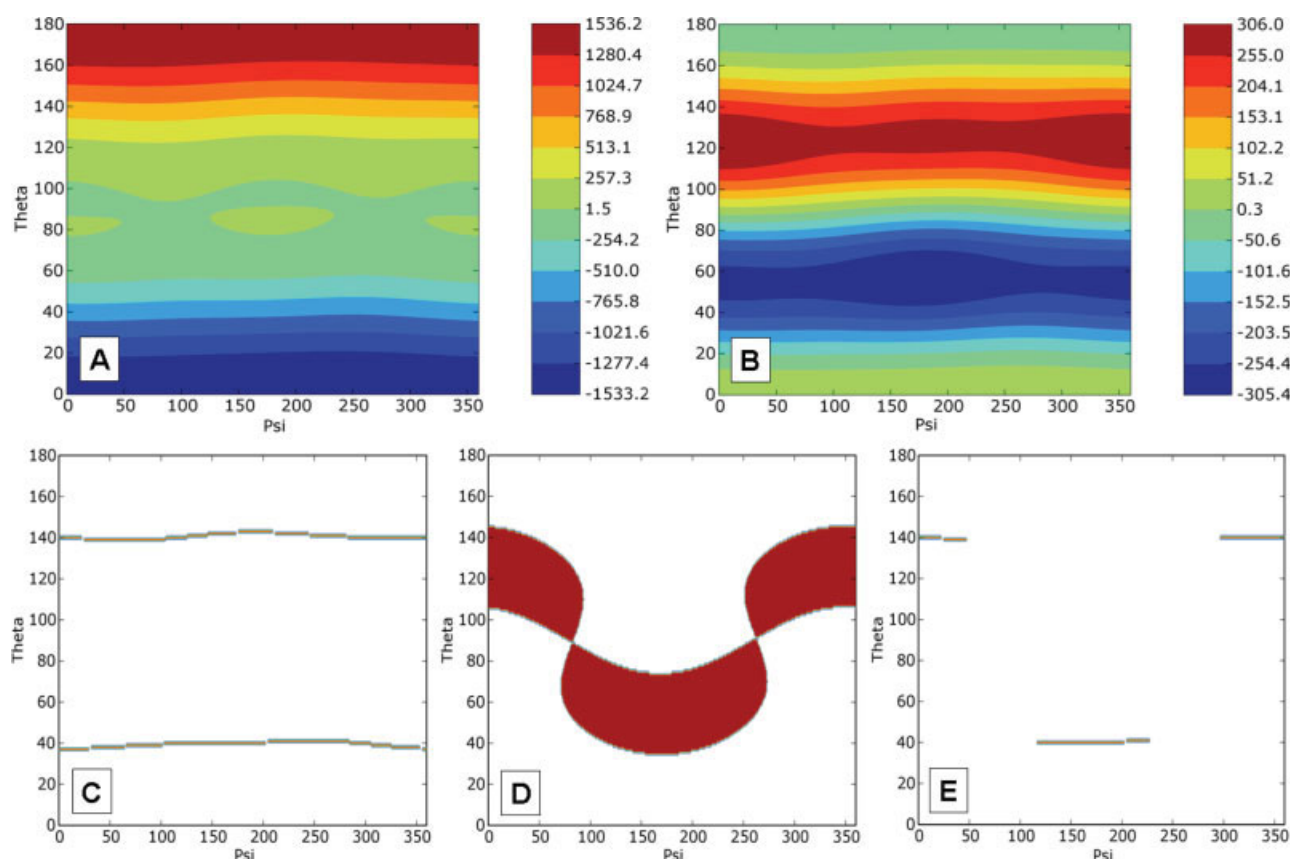


**Figure 5.** Predicted macroscopic tensor elements  $\chi_{ZZZ}$  (A) and  $\chi_{ZXX}$  (B) for SHG from DR-19 of  $\theta$  and  $\psi$  describing the tilt and twist angles, respectively. “Slices” through contour plots of  $\chi_{ZZZ}$  (C) and  $\chi_{ZXX}/\chi_{XXZ}$  (D) correspond to the range of values within  $2\sigma$  of the measured results. The overlapping regions shown in (E) of plots (C) and (D) correspond to the range of experimentally accessible tilt and twist angles in the limit of a narrow orientation distribution. [Color figure can be viewed in the online issue, which is available at [www.interscience.wiley.com](http://www.interscience.wiley.com).]

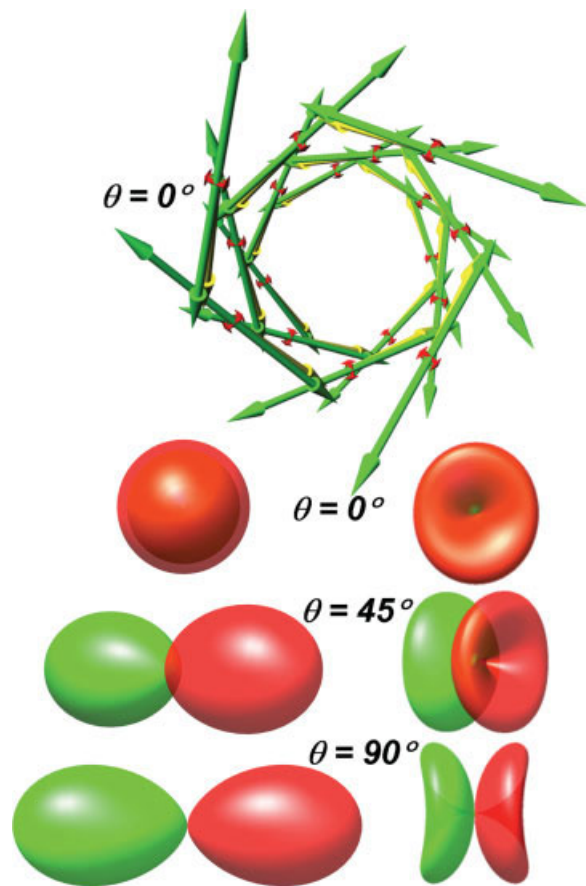


**Figure 6.** Diagrammatic and hyperellipsoid representations of the Amide I vibrational transitions of an  $\alpha$ -helix. The three hyperellipsoids to the left and right correspond to the excitation transition polarized parallel and perpendicular to the helix axis, respectively. The three hyperellipsoids on the right have been scaled up by 3.3 $\times$  for visual clarity. [Color figure can be viewed in the online issue, which is available at [www.interscience.wiley.com](http://www.interscience.wiley.com).]

DR-19 is an azobenzene push–pull chromophore with an electron withdrawing group on one end and an electron donating group on the other, which results in a nonlinear optical response that is dominated by interactions along the molecular long axis. Figure 3 shows the molecular structure of DR-19 and the diagrammatic representation of the transition moment  $\mu^{(0)}$  and two-photon polarizability tensor  $\alpha^{(1)}$  obtained from quantum calculations. A grid of different values of  $\theta$  and  $\psi$  are used to generate a contour plot spanning the full range of possible orientations. Examples of these contour plots are shown in Figures 5A and 5B for two of the nonzero macroscopic tensor elements  $\chi_{ZZZ}$  and  $\chi_{ZZX}$  for DR-19. These plotting capabilities can be used to help guide the interpretation of orientation information from experimental polarization measurements. Previous measurements of DR-19 produced reliable values for ratios of tensor elements.<sup>15</sup> The software is designed to allow algebraic combinations of surface tensors to be plotted as well, which facilitates direct comparisons with these experimental data.<sup>7</sup> The experimentally determined ratios  $\chi_{ZZZ}/\chi_{XXZ}$  and  $\chi_{ZZX}/\chi_{XXZ}$  with errors from ref. 15 can be plotted easily in *NLOPredict*. The measured values within experimental

error ( $2\sigma$ ) are shown in Figures 5C and 5D. The colored regions in Figure 5C and 5D correspond to slices through contour plots of tensor ratios qualitatively similar to those depicted in Figure 5A and 5B. In Figure 5E, the colored regions indicate the possible average orientation within experimental error of the DR-19 molecules on the surface in the limit of a narrow distribution. The intersection of these regions corresponding to the two measured ratios in Figure 5E indicates the range of possible orientations consistent with both experimentally determined ratios.

Inspection of the contour plots reveals interesting trends. In the limit of a narrow orientation distribution, the results indicate that the tilt angle is within  $2^\circ$  of the SHG magic angle of  $39.2^\circ$  away from  $0^\circ$  or  $180^\circ$ .<sup>16</sup> This result is consistent with both a very narrow distribution in tilt around  $39.2^\circ$  and a broad distribution in tilt angles. Because the absolute polar order cannot be unambiguously determined from ratios of the tensor elements, the measured values are consistent with orientations of  $39.2^\circ$  and  $140.8^\circ$ . Interestingly, there are regions of the twist angle that are inconsistent with measurements in the  $\delta$ -function limit. If the molecular tensor was dominated

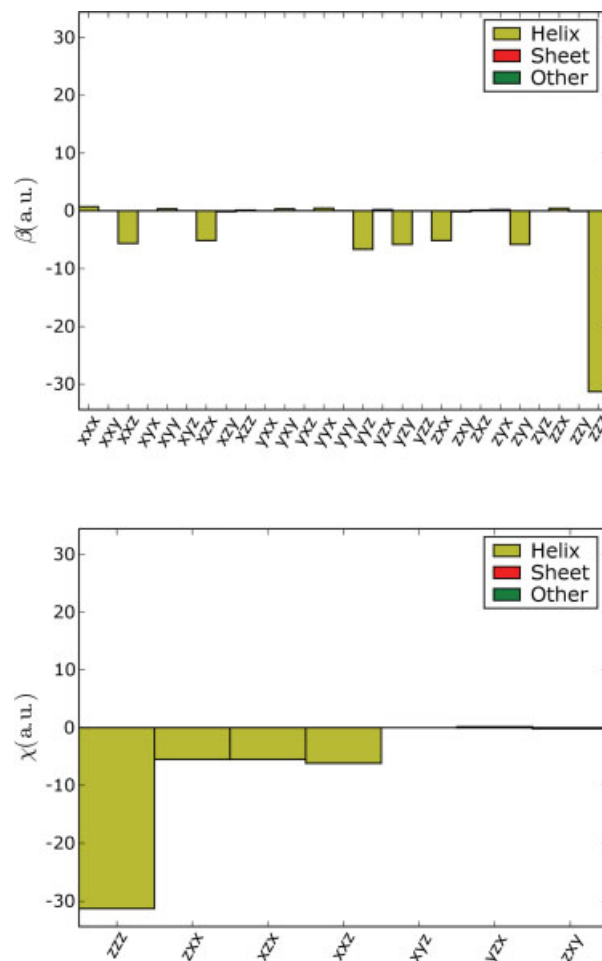


**Figure 7.** Bar chart plots of the molecular and macroscopic tensors for the model  $\alpha$ -helix displayed in Figure 6, oriented as shown. [Color figure can be viewed in the online issue, which is available at [www.interscience.wiley.com](http://www.interscience.wiley.com).]



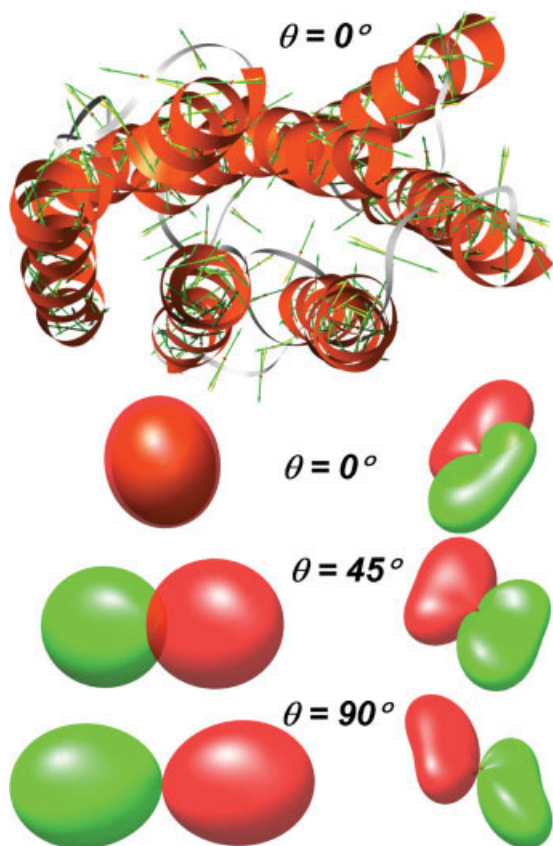


**Figure 8.** Diagrammatic and hyperellipsoid visualizations of the SFG tensor for Amide I transitions in the protein 2BRD. Hyperellipsoids on the left and right correspond to amides that a part of and not a part of  $\alpha$ -helices, respectively. The three hyperellipsoids on the right have been scaled up by  $1.5\times$  for visual clarity. [Color figure can be viewed in the online issue, which is available at [www.interscience.wiley.com](http://www.interscience.wiley.com).]

exclusively by interactions along a single internal axis, the final result would be independent of  $\psi$ . It is remarkable that previous measurements exhibited sufficient precision to allow assessment of the possible distribution in  $\psi$  in a rodlike chromophore like DR-19. However,  $\mu^{(0)}$  and the dominating component of  $\alpha^{(1)}$  have a small but nonzero angle between them, which allows the possibility of obtaining information on the twist angle from precise experimental measurements.

### Exciton Coupling in Protein Secondary Structural Motifs

The nonlinear optical properties of systems of many identical coupled chromophores can also be reliably calculated by *NLOPredict*. Coupling between chromophores generally results in splitting in energies for transitions polarized along the different pseudo-symmetry axes within different secondary structural motifs. From perturbation theoretical treatments,<sup>13</sup> the polarization-dependence of each exciton state can be estimated by projection of the  $\beta^{(2)}$  tensors for each monomer in a given macromolecule followed by separation of the resulting tensor elements into classes associated

with the different exciton states. In the limit of relatively strong coupling, the energy splitting between exciton states can be comparable to or greater than the full width at half maximum (FWHM) of the spectral peak. The local oscillator approximation is no longer strictly applicable in this limit.<sup>13</sup> Nevertheless, the polarization-dependent NLO properties of each individual exciton state can still be recovered by *NLOPredict*.

An example of this procedure is shown in Figures 6 and 7 for an  $\alpha$ -helix protein secondary structure. The backbone of a protein is comprised of amino acids linked by amide bonds. In polymers comprised of several identical repeated units, *NLOPredict* yields the set of tensors given by the coherent summation of all the monomer responses. By orienting the secondary structural motif with the symmetry axes corresponding to improper rotation positioned along the (X, Y, Z) axes in the viewing window, the influence of coupling can be introduced phenomenologically.<sup>13</sup> The resulting set of  $\beta^{(2)}$  tensor elements can be separated into classes based on the polarization-dependence of the transition moment, such that the set of transitions polarized along the macromolecular Z-axis correspond to the tensor

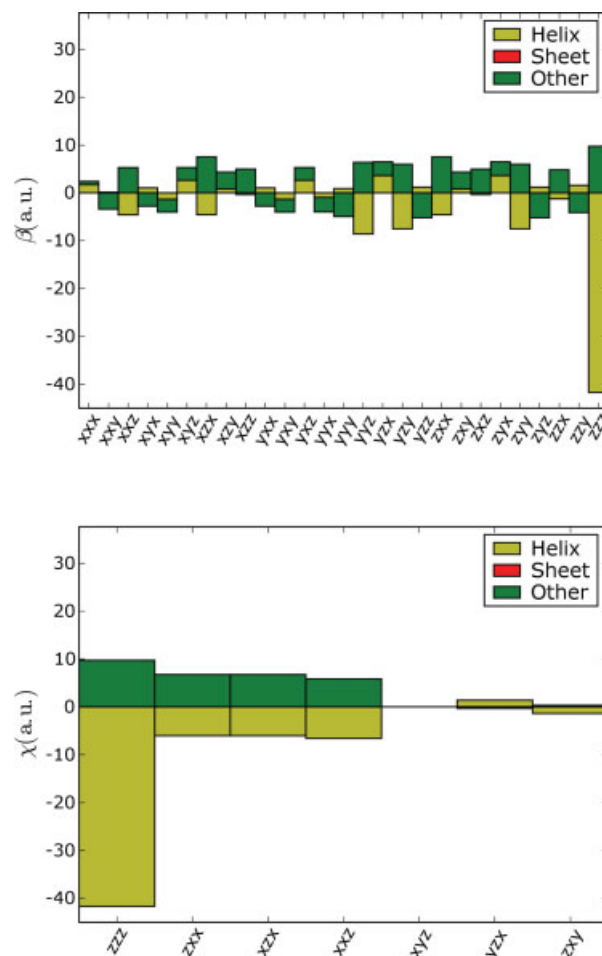


**Figure 9.** Bar chart representations of the molecular tensor and surface tensor of 2BRD divided into groups based on secondary structure for the orientation shown in Figure 8. [Color figure can be viewed in the online issue, which is available at [www.interscience.wiley.com](http://www.interscience.wiley.com).]

elements with an initial index of  $z$  when considering SHG and SFG resonant near the sum frequency and the elements ending with  $z$  for vibrational SFG. This simple projection and separation approach has previously been shown to reasonably recover both the sign and magnitude of the polarization-dependent NLO properties of different electronic and vibrational exciton states in protein secondary structures.<sup>13,17</sup>

This same general projection approach for treating exciton coupling can also be used for describing the isotropic SFG activities of different protein secondary structural motifs. Unlike SHG, SFG is symmetry allowed in chiral systems if the TPA or Raman tensor contains significant anti-symmetric contributions.<sup>5,18–20</sup> Specifically, the resonance-enhanced isotropic response is given by the dot product of the transition moment and the vector representation of the anti-symmetric TPA or Raman tensor.<sup>13</sup> In proteins, the isotropic vibrational and electronic amide chiroptical response can be reasonably assumed to be dominated by coupling interactions between nominally achiral chromophores. In this case, the isotropic response of the  $z$ -polarized exciton state near resonance at the sum frequency is given by  $\beta_{zxy} - \beta_{zyx}$  and the approximately equal and opposite response of the doubly degenerate  $x,y$ -polarized exciton state is given by  $\beta_{xyz} - \beta_{xzy} + \beta_{yxz} - \beta_{yzx}$  (for vibrational SFG, the isotropic activities of the two transitions are given by  $\beta_{xyz} - \beta_{yxz}$  and by  $\beta_{zxy} - \beta_{xzy} + \beta_{yzx} - \beta_{zyx}$ ). The isotropic SFG activities generated in this manner by *NLOPredict* (not shown) agree quantitatively with previous predictions from perturbation theory.<sup>13</sup>

### Biopolymers

If energetic contributions from coupling are relatively weak (i.e., the energy splitting from coupling is less than the FWHM of the monomer absorption peak), the macromolecular NLO properties are reasonably approximated by the coherent summation of the uncoupled monomer responses.<sup>13</sup> In this limit, the nonlinear optical properties of remarkably complex structures are straightforward to rapidly estimate. An example of this procedure is shown for the integral membrane protein bacteriorhodopsin (bR) in Figures 8 and 9. The amide NLO response of bR is dominated by the seven trans-membrane  $\alpha$ -helices. Because of the antiparallel arrangement of six of the  $\alpha$ -helices, the predicted net NLO response is remarkably similar to that shown in Figure 7 for an isolated  $\alpha$ -helix of comparable length. Interestingly, the chiral-specific macroscopic tensor elements  $\chi_{yzx}$  and  $\chi_{zxy}$  for bR is predicted to be  $\sim 7$  times larger than for the isolated  $\alpha$ -helix. While the achiral contributions cancel for anti-parallel  $\alpha$ -helices, the chiral contributions add. To facilitate similar analyses on complex proteins with known structures, *NLOPredict* is designed for convenient interfacing with the protein data bank.<sup>21</sup>

### Conclusion

*NLOPredict* is designed to facilitate the interpretation of experimental measurements and quantum chemical calculations of nonlinear optical phenomena with several enabling capabilities. At the molecular level, *NLOPredict* provides a convenient diagrammatic approach for visually representing nonlinear optical tensors in a coordinate-independent manner. Combining molecular-level information with experimental measurements of the macroscopic

polarization-dependent NLO activity allows for orientational analysis. Through exciton coupling perturbation theory, the NLO properties of protein secondary structures and complete proteins can be generated intuitively.

The software package described here represents an ongoing collaboration. In subsequent versions of *NLOPredict*, we hope to include capabilities to predict the nonlinear optical response for other polymeric assemblies besides protein backbones (e.g., DNA, aromatic side-chains). Additionally, the software package is being expanded to allow capabilities to include calculations for alternative linear and nonlinear optical processes, including Raman, multiphoton absorption, coherent anti-Stokes Raman, degenerate four-wave mixing, and hyper-Raman spectroscopies.

### References

- Chen, X.; Clarke, M. L.; Wang, J.; Chen, Z. *Int J Mod Phys B* 2005, 19, 691.
- Simpson, G. J. *ChemPhysChem* 2004, 5, 1301.
- Fischer, P.; Hache, F. *Chirality* 2005, 17, 421.
- Zipfel, W. R.; Williams, R. M.; Webb, W. W. *Nat Biotechnol* 2003, 21, 1369.
- Belkin, M. A.; Shen, Y. R. *Int Rev Phys Chem* 2005, 24, 257.
- Moad, A. J.; Simpson, G. J. *J Phys Chem A* 2005, 109, 1316.
- Moad, A. J.; Simpson, G. J. *J Phys Chem B* 2004, 108, 3548.
- Heinz, T. F. In *Nonlinear Surface Electromagnetic Phenomena*; Ponath, H.-E., Stegeman, G. I., Eds.; North-Holland: New York, 1991; 354–416; Vol. 29 of *Modern Problems In Condensed Matter Sciences*.
- Hirose, C.; Akamatsu, N.; Domen, K. *J Chem Phys* 1992, 96, 997.
- Hirose, C.; Akamatsu, N.; Domen, K. *Appl Spectrosc* 1992, 46, 1051.
- Petersen, E. F.; Goddard, T. D.; Huang, C. C.; Couch, G. S.; Greenblatt, D. M.; Meng, E. C.; Ferrin, T. E. *J Comput Chem* 2004, 25, 1605.
- Gaussian 98 (Revision A.9), Frisch, M. J.; Trucks, G. W.; Schlegel, H. B.; Scuseria, G. E.; Robb, M. A.; Cheeseman, J. R.; Zakrzewski, V. G.; Montgomery, Jr., J. A.; Stratmann, R. E.; Burant, J. C.; Dapprich, S.; Millam, J. M.; Daniels, A. D.; Kudin, K. N.; Strain, M. C.; Farkas, O.; Tomasi, J.; Barone, V.; Cossi, M.; Cammi, R.; Mennucci, B.; Pomelli, C.; Adamo, C.; Clifford, S.; Ochterski, J.; Petersson, G. A.; Ayala, P. Y.; Cui, Q.; Morokuma, K.; Malick, D. K.; Rabuck, A. D.; Raghavachari, K.; Foresman, J. B.; Cioslowski, J.; Ortiz, J. V.; Baboul, A. G.; Stefanov, B. B.; Liu, G.; Liashenko, A.; Piskorz, P.; Komaromi, I.; Gomperts, R.; Martin, R. L.; Fox, D. J.; Keith, T.; Al-Laham, M. A.; Peng, C. Y.; Nanayakkara, A.; Gonzalez, C.; Challacombe, M.; Gill, P. M. W.; Johnson, B. G.; Chen, W.; Wong, M. W.; Andres, J. L.; Head-Gordon, M.; Replogle, E. S.; Pople, J. A. *Gaussian, Inc.*, Pittsburgh PA, 1998.
- Perry, J. M.; Moad, A. J.; Begue, N. J.; Wampler, R. D.; Simpson, G. J. *J Phys Chem B* 2005, 109, 20009.
- Kielich, S. *IEEE J Quantum Electron* 1969, QE-5, 562.
- Plocinik, R. M.; Everly, R. M.; Moad, A. J.; Simpson, G. J. *Phys Rev B* 2005, 72, 125409.
- Simpson, G. J.; Rowlen, K. L. *J Am Chem Soc* 1999, 121, 2635.
- Simpson, G. J.; Perry, J. M.; Moad, A. J.; Wampler, R. D. *Chem Phys Lett* 2004, 399(1–3), 32.
- Fischer, P.; Wiersma, D. S.; Righini, R.; Champagne, B.; Buckingham, A. D. *Phys Rev Lett* 2000, 85, 4253.
- Belkin, M. A.; Kulakov, T. A.; Enrst, K.-H.; Yan, L.; Shen, Y. R. *Phys Rev Lett* 2000, 85, 4474.
- Giordmaine, J. A. *Phys Rev A* 1965, 138, 1599.
- Berman, H. M.; Westbrook, J.; Feng, Z.; Gilliland, G.; Bhat, T. N.; Weissig, H.; Shindyalov, I. N.; Bourne, P. E. *Nucl Acids Res* 2000, 28, 235.